buildings

MDPI

Article

Controlling Performance and Parameters Investigation of the Improved Mega-Sub Controlled Structural System (MSCSS) for a Tall Building

Mustapha Abdulhadi [1,2,*], Zhang Xun'an [1], Buqiao Fan [3], Sadi Ibrahim Haruna [4,*] and Yasser E. Ibrahim [4]

[1] School of Mechanics, Civil Engineering and Architecture, Northwestern Polytechnical University, Xi'an 710072, China; jiaoping@npu.edu.cn
[2] Department of Civil Engineering, Air Force Institute of Technology (AFT), Nigerian Air Force, P.M.B. 2104, Kaduna 800283, Nigeria
[3] Department of Civil Engineering, North China University of Water Resources and Electric Power, Zhengzhou 450046, China; buqiao@mail.nwpu.edu.cn
[4] Engineering Management Department, College of Engineering, Prince Sultan University, Riyadh 11586, Saudi Arabia; ymansour@psu.edu.sa
* Correspondence: mustapha.a@chula.ac.th (M.A.); sharuna@psu.edu.sa (S.I.H.)

Abstract

The study presented a newly proposed mega-sub controlled structure system (MSCSS), connected to the design and building of high-rise structures, as enhanced durability and efficiency of mega-structural frames attracted the attention of researchers. In this article, a more reasonable and advanced mega-sub controlled structure model is designed and investigated under wind load. The complex model analysis theory is used to generate the equations of motion, the response spectrum (RS) expression, and the mean square response (MSR). The dynamic features that influence the control response of MSCSS, such as relative stiffness ratio (RD) and relative mass ratio (MR) between the mega-frame and substructure, are defined and investigated. The result showed that the displacement effectiveness is highly effective at low stiffness ratios, with a sharp decrease in maximum displacement observed when RD is less than 0.17 (RD < 0.17). Optimal response control effectiveness was identified within the RD range of 0.17 to 0.6. Also, the result indicates better acceleration control effectiveness when RD is between 0.3 and 0.5; however, this control decreases significantly when RD > 0.6. Furthermore, the study reveals that increasing the relative mass ratio obviously improves both displacement and acceleration control effectiveness at fixed RD = 0.3.

Keywords: mega substructures; MSCSS; displacement; wind load; tall building

Check for updates

Academic Editor: Agathoklis Giaralis

Received: 3 February 2026
Revised: 20 March 2026
Accepted: 26 March 2026
Published: 28 March 2026

Copyright: © 2026 by the authors. Licensee MDPI, Basel, Switzerland. This article is an open access article distributed under the terms and conditions of the Creative Commons Attribution (CC BY) license.

1. Introduction

Wind load is one of the critical loads that must be considered in the design of high-rise buildings. Wind load's influence as a natural phenomenon on tall and super-tall buildings cannot be ignored. It is seen in many design cases that terrible condition occurs under wind load for high-rise buildings. The traditional way to suppress the structure's reaction to the wind load is to increase its stiffness; thus, this significantly increases the price of building the structure [1]. The wind load is essential in the analysis and design of tall buildings. Previous research [2–5] investigated the action of tall building structures under wind and seismic loading, applying many configurations of the tall structures to minimize the lateral load effect, including frame–tube with a connecting steel truss [6], double-skin

facades [7], diagrid core–tube [8], core–outrigger [9], crumb rubber [10], etc. Several tall building patterns were explored by [11]. Recently, Hogue and Hossain [12] developed a Numerical model for investigating the behavior of concrete-encased steel tube columns in tall buildings exposed to wind load. The author reported that the CEST exhibits greater stiffness fluctuations and less deflection than the control RC column. Jeong et al. [13] proposed a novel regenerated coherence (RC) technique to develop 3D wind load time histories applying high-frequency force balance (HFFB), while taking coherences across various directions and levels into account. Recently, Forcellini and Kalfas [14] study interstory seismic isolation strategies for high-rise buildings. Abdulhadi et al. [15] proposed Hybrid VD-TFPB Control System with Consideration of Soil Structure Interaction to improve the control effectiveness of high rise buildings.

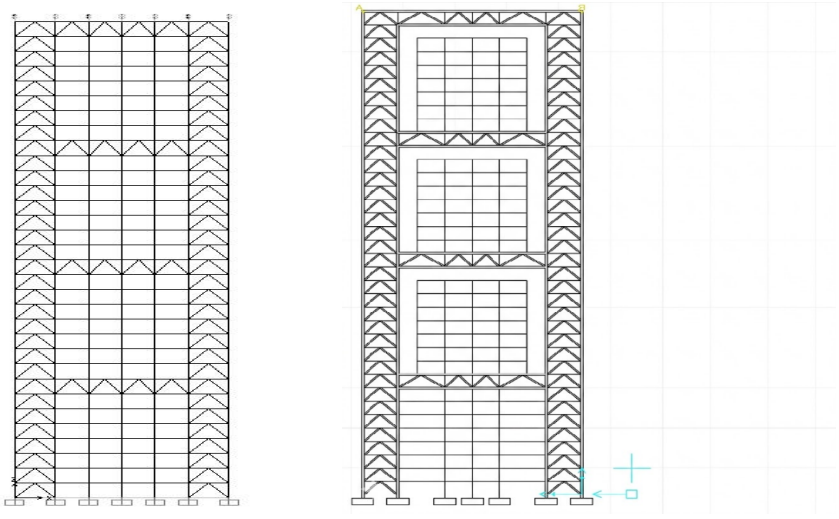
Additionally, tuned mass damper systems (TMD) have been used in conventional structures and were effective in improving their dynamic responses under the wind. Another critical and cost-effective way to reduce the building vibration is to form a new assembly based on an MSS arrangement. This new form of design is called mega-sub controlled structural (MSCS). In 1995, the MSCS system was initially introduced into the tall building by Feng and Mita [16] through releasing the connections between the mega-frame and the sub-frame. Subsequently, two years later, the MSCS system was amended by Chai and Feng [17], using a concentrated mass and a cantilever beam to characterize a substructure and a mega-structure, respectively. A non-white technique involving noise stochastic was used to investigate the dynamic response caused by random wind load excitation. A study demonstrated a multi-functional mega sub-frame with an ideal base system and a TMD influence [16]. The improved controlled structure of the MSCSS was idealized [18]. In their arrangement, dampers were introduced between the mega-structure and sub-frame to enhance the control efficiency of the structures. Moreover, an additional column (AC) is added at the highest level of the sub-frame of each mega-frame to solve optimization problems associated with both the mega beam's and the mega beam floor's excessive length. The analysis results showed that the enhanced MSCSS configuration can supply a huge amount of energy for structural control and is very efficient in decreasing the structure's acceleration and displacement responses. In another development, a friction damper was used in MSCSS to moderate substructure performance and improved the comfort and security of the building under wind forces [19]. The result showed that the resistance capability of an improved MSCSS exceeds traditional mega-substructures. The parametric investigation of the building behavior as an active tools for controlling the seismic behavior of MSCSS was conducted by Zhang et al. [20]. The authors analyzed different controlling techniques and compared the results with MSS. The findings showed that MSCSS improves structural safety while decreasing structural acceleration and displacement under wind load. Significant improvement has been made recently with regard to the design and analysis of MSCSS under earthquake ground motion [21–24]. However, there are still some issues with its design that need to be addressed before the proposed arrangement can be implemented. For example, in the improved arrangement previously presented by Zhang et al. [20] and improved by Abdulhadi et al. [22], the control performance of the additional column required has been changed to better the interaction with the mega floor beam that could affect control. Furthermore, the arrangement and location of the damper have a significant impact on the control effectiveness of MSCSS. A high damping coefficient (C) pushes the greater damping forces outside the system's capabilities, reducing the structure's control effectiveness significantly. However, this improvement has been investigated under earthquake load, and needs to be studied under wind load.

In this study, the improved MSCSS model, previously improved by [22,25] was built and investigated under wind load effect based on the MSCSS control mechanism. The study

introduces rubber bearings at the highest level of the AC to enhance the control behavior of the AC and mega floor beam, and the overall response of the tall building structures. Under unexpected wind load, the corresponding dynamic equation of the system is obtained using the complex model analytical method of random vibration. The study employed the Davenport wind speed spectrum, and wind coherence was taken into account. The RS expression and MSR are obtained from acceleration and displacement. The control response of the system with respect to relative mass and relative stiffness between the mega-structure and the sub-frame is investigated. Furthermore, the structural frequency on the MSCSS, which is one of the most important parameters that describes the structural dynamical characteristics, was investigated.

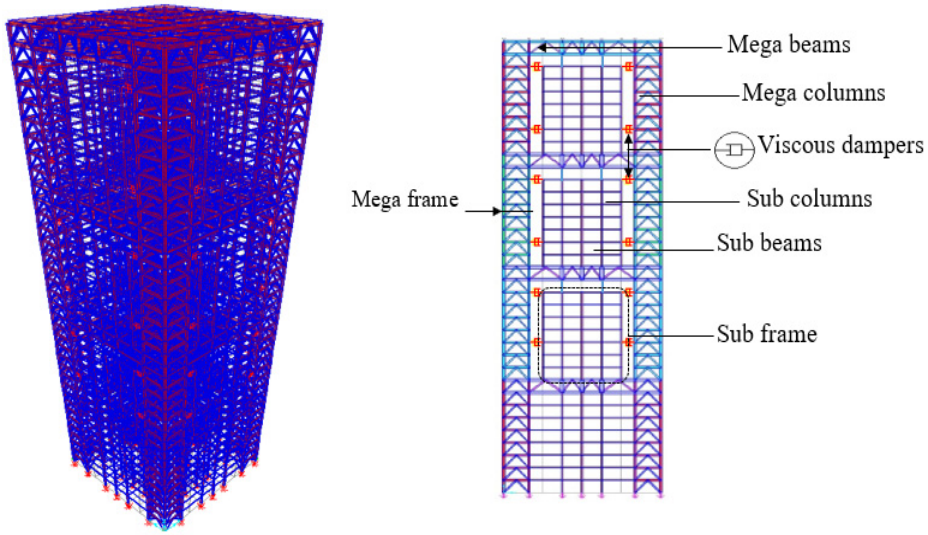
2. Analytical Model and Equation of Motion of MSCSS

The conventional mega-substructure is shown in Figure 1a, where the mega-frame serves as the main structure, consisting of structural elements (beams and columns) to which several sub-frames are connected. Each substructure is typically connected to the mega-frame and has 10–12 stories for steel mega-frames or 4 to 6 stories for reinforced concrete mega-frames. The MSCSS configuration is shown in Figure 1b, in which the concrete structure consists of a mega-frame and several isolated sub-frames resting on a mega beam Figure 1b, used for stories and residential purposes. In any structure, bending is regarded as the principal vibration response for the mega-structure, and shear deformation is regarded as the prevailing mode for the sub-frame. Hence, the analyzed model for improved MSCSS can be represented as the MDOF system displayed in Figure 1b. As stated before, the recommended MSCSS would consist of a substructure arranged such that the energy between the mega-frame and sub-frame can be used to show the vibration of the structures. The sub-frame is composed as a controlled sub-frame and connected to the mega beam. Moreover, an AC was added, and a LRB was placed at the top surface of it to reduce the constraint [16], which also led to the reduction in the performance behavior and the whole structure, illustrated in Figure 1b. In the second to fourth mega floors, a pair of viscous dampers was installed.



(**a**)

Figure 1. *Cont.*



(**b**)

Figure 1. MSS and MSCSS arrangements. (**a**) Illustration models (MSS and MSCSS). (**b**) An illustration of the MSCSS model details (close-up view).

The model equation of the MSCSS can be derived when a single concentrated mass represents individual stories, and the building is converted into a set of lumped masses (Figure 2b). The traditional MSS is presented in Figure 2a. An MSCSS with n mega floors and ns sub-frames, consisting of nz floors shifting relative to the main frame, amounting to N = n + ns + nz degree freedom. Therefore, the improved MSCSS's dynamic expression can be stated in Equations (1)–(4).

$$\mathbf{M}\frac{d^2\mathbf{x}(t)}{dt^2} + \mathbf{C}\frac{d\mathbf{x}(t)}{dt} + \mathbf{K}\mathbf{x}(t) = \mathbf{f}(t) \tag{1}$$

where $\mathbf{x} = [\mathbf{x_p^T}, \mathbf{x_1^T}, \mathbf{x_2^T}, \mathbf{x_3^T} \ldots\ldots \mathbf{x_n^T}]^T$ represent the building deformation vector, and $\mathbf{x_p^T}, \mathbf{x_i^T}(i = 1, 2, 3 \ldots\ldots n_s)$ are the mega-frame and i^{th} substructure deformation vectors, respectively [6]. The vector $F(t)$ represent the random wind loads operating on the buildings [26].

The mass matrix M in Equation (1) can be stated as:

$$\mathbf{M} = diag[\mathbf{M_P}, \mathbf{M_1}, \mathbf{M_2}, \mathbf{M_3}, \ldots\ldots \mathbf{M_i}, \ldots\ldots \mathbf{M_{ns}}] \tag{2}$$

where $\mathbf{M_P}$ is the $n \times n$ mega-structure diagonal matrix, and $\mathbf{M}_i(i = 1, 2, \ldots\ldots n_s)$ is the $n_z \times n_z$ i^{th} Sub-frame diagonal matrix.

From (1), K is the stiffness matrix and can be expressed as:

$$\mathbf{K} = \begin{pmatrix} \mathbf{K_P} + \mathbf{K_{s,diag}} & \mathbf{K_c} \\ \mathbf{K_c^T} & \mathbf{K_s} \end{pmatrix}$$
$$\mathbf{K_s} = \mathbf{diag}[\mathbf{K_{s,1}}, \mathbf{K_{s,2}}, \mathbf{K_{s,3}}, \ldots\ldots \mathbf{K_{s,i}}, \ldots\ldots \mathbf{K_{s,ns}}] \tag{3}$$

where $\mathbf{K_P}$ is the $n \times n$ mega-structural stiffness, $\mathbf{K_{s,i}}(i = 1, 2, \ldots\ldots n_s)$ is the $n_z \times n_z$ stiffness matrix of the i^{th} substructures

$$\mathbf{K_{si}} = \begin{bmatrix} K_{i,1} + K_{i,2} & -K_{i,2} & 0 & 0 & \ldots & 0 \\ -K_{i,2} & K_{i,2} + K_{i,3} & -K_{i,3} & 0 & \ldots & 0 \\ \vdots & \vdots & \ddots & \ddots & \ddots & \vdots \\ 0 & 0 & 0 & -K_{i,nz-1} & K_{i,nz-1} + K_{i,nz} & -K_{i,nz} \\ \vdots & \vdots & \vdots & \vdots & \vdots & \vdots \\ 0 & 0 & \ldots & 0 & -K_{i,nz} & K_{i,nz} \end{bmatrix}_{nz \times nz} \tag{4}$$

where ki,1 (i = 1, 2, …, n1) is the shear stiffness value of the ith substructure. The matrix **Kc** in Equation (3) is the parameter connecting the mega-structure and the substructures and has n x n1nz matrix elements.

$$\mathbf{K}_c = \begin{array}{c} \\ 1 \\ 2 \\ \vdots \\ \\ \vdots \\ i \\ \vdots \\ n1 \\ \vdots \\ \\ \vdots \\ \\ \vdots \\ n \end{array} \begin{bmatrix} 1 & 2 & \dots & n_z+1 & \dots & 2n_z+1 & \dots & (i-1)n_z+1 & \dots & (n_1-1)n_z+1 & \dots & n_1n_z \\ -K_{1,1} & 0 & \dots & 0 & \dots & 0 & \dots & 0 & \dots & 0 & \dots & 0 \\ 0 & 0 & \dots & 0 & \dots & 0 & \dots & 0 & \dots & 0 & \dots & 0 \\ \vdots & \vdots & \vdots & -K_{2,1} & \vdots & \vdots & \vdots & \vdots & \vdots & \vdots & \vdots & \vdots \\ 0 & 0 & \dots & 0 & \dots & -K_{3,1} & \dots & 0 & \dots & 0 & \dots & 0 \\ 0 & 0 & \dots & 0 & \dots & \dots & \dots & -K_{i,1} & \dots & 0 & \dots & 0 \\ \vdots & \vdots & \vdots & \vdots & \vdots & \vdots & \vdots & \vdots & \vdots & \vdots & \vdots & \vdots \\ 0 & 0 & \dots & 0 & \dots & 0 & \dots & 0 & \dots & -K_{n,1} & \dots & 0 \\ 0 & 0 & \dots & 0 & \dots & 0 & \dots & 0 & \dots & 0 & \dots & 0 \\ \vdots & \vdots & \vdots & \vdots & \vdots & \vdots & \vdots & \vdots & \vdots & \vdots & \vdots & \vdots \\ 0 & 0 & \dots & 0 & \dots & 0 & \dots & 0 & \dots & 0 & \dots & 0 \\ 0 & 0 & \dots & 0 & \dots & 0 & \dots & 0 & \dots & 0 & \dots & 0 \\ 0 & 0 & \dots & 0 & \dots & 0 & \dots & 0 & \dots & 0 & \dots & 0 \end{bmatrix}_{n1n2} \tag{5}$$

In addition, the sub matrix $K_p + K_{s,diag}$ of Equation (3) can be assembled in the following form

$$\mathbf{K_P+K_{s,diag}} = \begin{bmatrix} K_{P1,1}+K_{1,1} & K_{P1,2} & \dots & K_{P1,i} & \dots & K_{P1,n-1} & K_{P1,n} \\ K_{P2,1} & K_{P2,2}+K_{2,1} & \dots & K_{P2,i} & \dots & K_{P2,n-1} & K_{P2,n} \\ \vdots & \vdots & \ddots & \vdots & \ddots & \vdots & \vdots \\ K_{Pi,1} & K_{Pi,2} & \dots & K_{Pi,i}+K_{i,1} & \dots & K_{Pi,n-1} & K_{Pi,n} \\ \vdots & \vdots & \ddots & \vdots & \ddots & \vdots & \vdots \\ K_{Pn-1,1} & K_{Pn-1,2} & \dots & K_{Pn-1,i} & \dots & K_{Pn-1,n-1}+K_{n1,1} & K_{Pn-1,n} \\ K_{Pn,1} & K_{Pn,2} & \dots & K_{Pn,i} & \dots & K_{Pn,n-1} & K_{Pn,n} \end{bmatrix}_{n\times n} \tag{6}$$

where $K_{pi,j}$ (i,j = 1, 2, 3, …, n) is the item of the stiffness matrix Kp of the mega-structure, and $K_{i,1}$ (i = 1, 2, 3, …, n1) is the shear stiffness value of the ith substructure.

Also, from (1), the damping matrix is given:

$$\mathbf{C}=\begin{pmatrix} \mathbf{C_P+C_{s,diag}} & \mathbf{C_c} \\ \mathbf{C_c^T} & \mathbf{C_s} \end{pmatrix}$$
$$\mathbf{C_s} = diag[\mathbf{C_{s,1}}, \mathbf{C_{s,2}}, \mathbf{C_{s,3}}, \dots\dots \mathbf{C_{s,i}}, \dots\dots \mathbf{C_{s,ns}}] \tag{7}$$

where $\mathbf{C_P}$ is the $n \times n$ mega-structure's damping matrix, and $\mathbf{C_{s,i}}(i = 1, 2, 3, \dots\dots n_s)$ is the $n_z \times n_z$ i^{th} sub-frame's damping matrix.

$$\mathbf{C_{si}} = \begin{bmatrix} C_{i,1}+C_{i,2} & -C_{i,2} & 0 & 0 & \dots & 0 \\ -C_{i,2} & C_{i,2}+C_{i,3} & -C_{i,3} & 0 & \dots & 0 \\ \vdots & \vdots & \ddots & \ddots & \ddots & \vdots \\ 0 & 0 & 0 & -C_{i,nz-1} & C_{i,nz-1}+C_{i,nz} & -C_{i,nz} \\ \vdots & \vdots & \vdots & \vdots & \vdots & \vdots \\ 0 & 0 & \dots & 0 & -C_{i,nz} & C_{i,nz} \end{bmatrix}_{nz\times nz} \tag{8}$$

$$\mathbf{C_c} = \begin{array}{c} \\ 1 \\ 2 \\ \vdots \\ \\ \vdots \\ \\ i \\ \vdots \\ n1 \\ \vdots \\ \\ \vdots \\ \\ \vdots \\ n \end{array} \begin{bmatrix} 1 & 2 & \dots & n_z+1 & \dots & 2n_z+1 & \dots & (i-1)n_z+1 & \dots & (n_1-1)n_z+1 & \dots & n_1n_z \\ -C_{1,1} & 0 & \dots & 0 & \dots & 0 & \dots & 0 & \dots & 0 & \dots & 0 \\ 0 & 0 & \dots & 0 & \dots & 0 & \dots & 0 & \dots & 0 & \dots & 0 \\ \vdots & \vdots & \vdots & -C_{2,1} & \vdots & \vdots & \vdots & \vdots & \vdots & \vdots & \vdots & \vdots \\ 0 & 0 & \dots & 0 & \dots & -C_{3,1} & \dots & 0 & \dots & 0 & \dots & 0 \\ 0 & 0 & \dots & 0 & \dots & \dots & \dots & -C_{i,1} & \dots & 0 & \dots & 0 \\ \vdots & \vdots & \vdots & \vdots & \vdots & \vdots & \vdots & \vdots & \vdots & \vdots & \vdots & \vdots \\ 0 & 0 & \dots & 0 & \dots & 0 & \dots & 0 & \dots & -C_{n,1} & \dots & 0 \\ 0 & 0 & \dots & 0 & \dots & 0 & \dots & 0 & \dots & 0 & \dots & 0 \\ \vdots & \vdots & \vdots & \vdots & \vdots & \vdots & \vdots & \vdots & \vdots & \vdots & \vdots & \vdots \\ 0 & 0 & \dots & 0 & \dots & 0 & \dots & 0 & \dots & 0 & \dots & 0 \\ 0 & 0 & \dots & 0 & \dots & 0 & \dots & 0 & \dots & 0 & \dots & 0 \\ 0 & 0 & \dots & 0 & \dots & 0 & \dots & 0 & \dots & 0 & \dots & 0 \end{bmatrix}_{n1n2} \tag{9}$$

$$\mathbf{C_P+C_{s,diag}} = \begin{bmatrix} C_{P1,1}+C_{1,1} & C_{P1,2} & \dots & C_{P1,i} & \dots & C_{P1,n-1} & C_{P1,n} \\ C_{P2,1} & C_{P2,2}+C_{2,1} & \dots & C_{P2,i} & \dots & C_{P2,n-1} & C_{P2,n} \\ \vdots & \vdots & \ddots & \vdots & \ddots & \vdots & \vdots \\ C_{Pi,1} & C_{Pi,2} & \dots & C_{Pi,i}+C_{i,1} & \dots & C_{Pi,n-1} & C_{Pi,n} \\ \vdots & \vdots & \ddots & \vdots & \ddots & \vdots & \vdots \\ C_{Pn-1,1} & C_{Pn-1,2} & \dots & C_{Pn-1,i} & \dots & C_{Pn-1,n-1}+C_{n1,1} & C_{Pn-1,n} \\ C_{Pn,1} & C_{Pn,2} & \dots & C_{Pn,i} & \dots & C_{Pn,n-1} & C_{Pn,n} \end{bmatrix}_{n\times n} \tag{10}$$

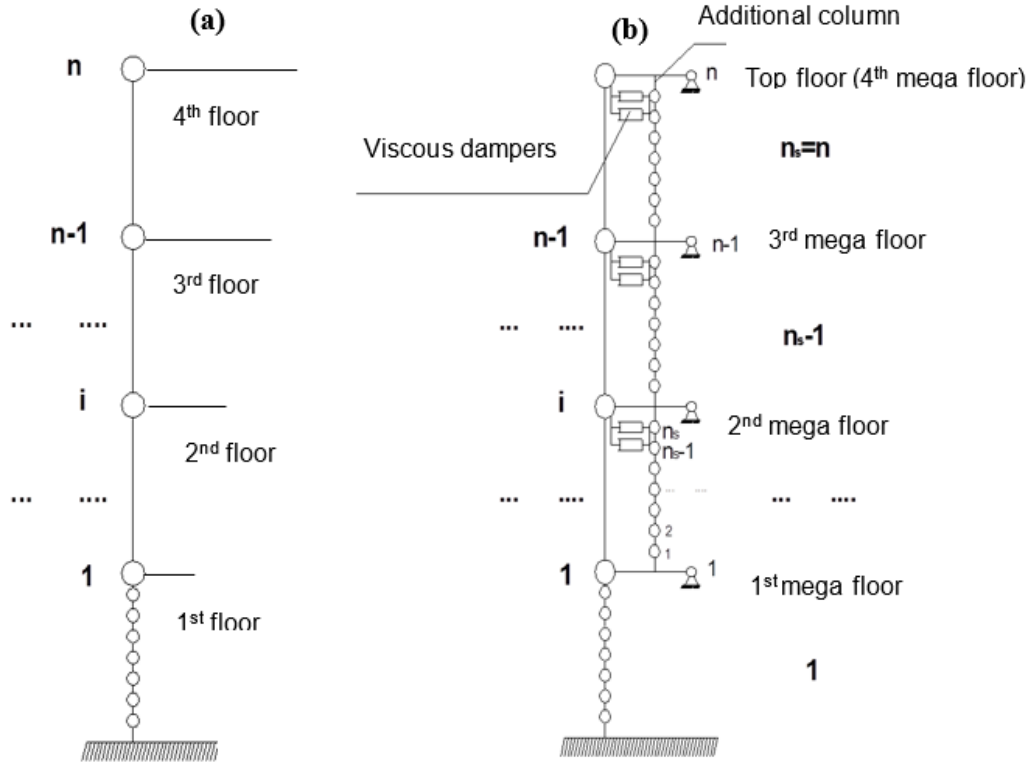


Figure 2. Lumped mass model for (**a**) MSS and (**b**) MSCSS.

The primary difference between the mega-substructure (MSS) and the mega-sub controlled structure (MSCSS) lies in how the sub-frames are connected to the mega-frame and how the energy dissipation is modeled in the governing equations. Although both models utilize the general equation of motion $\mathbf{M}\frac{d^2\mathbf{x}(t)}{dt^2} + \mathbf{C}\frac{d\mathbf{x}(t)}{dt} + \mathbf{K}\mathbf{x}(t) = \mathbf{f}(t)$, the composition of the damping and stiffness matrices differs based on the structural control strategy. Though the MSS matrix assembly looks like that of MSCSS, the values and physical meanings of the coupling terms differ as follows:

- In the MSS, $\mathbf{K_{s,diag}}$ represents a very high "bonded" stiffness or a direct structural connection between the mega beams and the substructure. In the MSCSS, $\mathbf{K_{s,diag}}$ is a tuned stiffness designed to allow controlled movement.
- In the MSS, the coupling term $\mathbf{C_{s,diag}}$ represents only the inherent structural damping of the joints. It lacks the large value $\mathbf{C_{s,diag}}$ MSCSS provided by the viscous dampers seen in the MSCSS diagrams.
- Because the MSS is more rigid, the entire building (Mega + Sub) typically has a higher fundamental frequency and moves as a single unit. In the MSCSS, the substructures move out of phase to act as absorbers.

2.1. Finite Element Modeling

The structural modeling is based on the idea that the floor is completely rigid within its own plane, which is called a "rigid floor assumption." The modeling process involves four main steps: creating the geometric model, describing the material properties, assigning the loads that would be applied, and performing thorough structural calculations. In addition, the development of the finite element model (FEM) is described in detail in three main sections: (i) specific modeling parameters, (ii) the use of viscous dampers, and (iii) the verification of the numerical model.

2.1.1. Modeling Details

SAP2000 V.21 is used to generate finite element models of the MSCS. These models use FEMA-356-compliant plastic hinges to demonstrate how nonlinear interactions occur in bracing and beam–column connections. To ensure that the simulation is correct, it incorporates both material and geometric nonlinearities, such as P-Delta effects. The behavior of steel is modeled using a trilinear constitutive model. To divide structural components into smaller pieces, we employ shell elements for slabs and frame elements for columns and beams. An automated meshing feature generates intermediate nodes. Numerical convergence occurs when the energy standard falls below 10^{-3}, maintaining force balance. The design loads are 2.0 kN/m^2 for live loads, and 6.0 kN/m^2 for dead loads. The structure is 144 m tall and 40 m wide, with mega-columns at the corners and floors that are firmly coupled to each other to form a cantilever-like structural system. These mega beams are made up of rigid vertical and horizontal elements connected by diagonal bracing. The mega-floor elements share the same sectional features as the main structure's sub-beams and sub-columns. Table 1 and Figure 1 illustrate the exact dimensions of the components, as well as how the viscous dampers are configured.

Table 1. Model parameters and properties of elements.

	Symbol	**Dimensions**	**Moment of Inertia**	
Members		**(X 10^{-3} m)**	**I_x (m^4)**	**I_y (m^4)**
Mega-column (1st and 2nd Floor)	P1 and P2	600 X 600 X 60 X 60	6.376×10^{-3}	6.376×10^{-3}
Mega-column (3rd Floor)	P3	600 X 600 X 40 X 40	4.707×10^{-3}	4.707×10^{-3}
Mega-column (4th Floor)	P4	600 X 600 X 20 X 20	2.605×10^{-3}	2.605×10^{-3}
Mega beam (1st and 2nd Floor)	B1 and B2	H1000 X 350 X 25 X 16	5.303×10^{-3}	1.790×10^{-4}

Table 1. *Cont.*

Members	Symbol	Dimensions (X 10^{-3} m)	Moment of Inertia	
			I_x (m^4)	I_y (m^4)
Mega beam (3rd and 4th Floor)	B2	H1000 X 350 X 25 X 15	5.232×10^{-3}	1.789×10^{-4}
Sub-column	Cs	430 X 430 X 10 X 10	4.942×10^{-3}	4.942×10^{-4}
Sub-beam element	Bs	H350 X 250 X 10 X 10	1.745×10^{-4}	2.607×10^{-5}
Mega beam brace	Bb1-4	350 X 350 X 20 X 20	4.809×10^{-4}	4.809×10^{-4}
Mega-column brace	Pb1-4	250 X 250 X 14 X 14	1.231×10^{-4}	1.231×10^{-4}
Additional column	Pa	430 X 430 X 10 X 10	4.942×10^{-3}	4.942×10^{-4}

2.1.2. Viscous Damper

The viscous dampers are designed using the Maxwell restoring model. The damping force is defined as $F_d = C_v|V_d|^{\alpha}\mathrm{sgn}(V_d)$, where C_v is the damping coefficient, V_d is the velocity, and alpha is the damping exponent. Seismic damping exponents typically range from 0.1 to 1.0. However, for structures that require quick energy dissipation, values below 0.4 are recommended. Thus, this study used a damping coefficient of 15 kNs/m and an exponent of 0.3. Figure 1 depicts the MSCSS configuration, which consists of four mega-stories, each with seven subfloors. The second, third, and fourth mega-levels each have a pair of dampers.

2.2. Response Spectrum (RS) and Mean Square Response (MSR) of MSCSS

From Equation (1), the matrix C given in Equation (4) with the introduction of damper influences cannot be decoupled because the condition needed for decoupling, as shown in Equation (1), Caughey and Kelly [27].

$$\mathbf{CM^{-1}K=KM^{-1}C} \tag{11}$$

The structural damping is modeled as non-proportional. This is due to the integration of discrete viscous dampers governed by the Maxwell restoring model, which introduces concentrated damping forces that do not satisfy the Caughey–Kelly condition. Consequently, the system is analyzed using complex mode analysis to account for the lack of classical proportionality and accurately capture the dynamic interactions. Therefore, to decouple and determine its solution, a complex model analytical method must be used [28]. The random wind load is represented by the Davenport wind speed spectrum.

After describing a state vector $\mathbf{r}=[\mathbf{x^T},\mathbf{x^T}]^{\mathbf{T}}$.

The motion equation, Equation (1), can then be written as:

$$\mathbf{Z(t)}=\left\{\mathbf{x(t)},\frac{\mathbf{dx(t)}}{\mathbf{dt}}\right\}^{\mathbf{T}} \tag{12}$$

where M_r and K_r are the mass and stiffness matrix, respectively, as presented in Equation (13)

$$\mathbf{M_r}=\begin{bmatrix}\mathbf{0} & \mathbf{M}\\ \mathbf{M} & \mathbf{C}\end{bmatrix},\ \mathbf{K_r}=\begin{bmatrix}-\mathbf{M} & \mathbf{0}\\ \mathbf{0} & \mathbf{K}\end{bmatrix} \tag{13}$$
$$\frac{dZ(t)}{dt} = AZ(t) + Bf(t)$$

Additionally, the decoupling equation can be expressed as follows by considering the orthogonality of the model matrices and applying complex model transformation principles:

$$Z - P_i \times Z_i = {m_i}^{*-1}{V_i}^T F(t),\ i = 1,2,3,\ldots\ldots 2N \tag{14}$$

$$m_i^* = V_i^T[2PM + C]\cdot u_i \tag{15}$$

2.3. Expression of the Displacement Power Spectrum Response

Using Duhamel integration, Equation (14) is given as:

$$Z_i(t) = \int_{-\infty}^{\infty} h(t-\mu){m_i}^{t-1}V_i^T F(\mu)\delta\mu,\ i = 1,2,3,\ldots\ldots 2N \tag{16}$$

Also, the cross-variance function of $Z_i(t)$ and $Z_j(t)$ can be determined from

$$E\left[Z_i(t_1)\overline{Z}_j^T(t_2)\right] = \int_{-\infty}^{\infty} H_i(-w){m_i}^{t-1}V_i^T[S_{F_K}F_L(w)] \times V_j\overline{m_i}^{1-T}{\overline{H}_j}^T(-w)e^{jw(t_2-t_1)}\delta w \tag{17}$$

In which $H(-w)$ and $\overline{H}(-w)$ represent the frequency function of –w and frequency conjugate function of $-w$, respectively, and can be expressed as:

$$H_i(-w) = \int_{-\infty}^{\infty} h_i(t_1-\mu_1)e^{iw(t_1-\mu_1)}\delta\mu_1 \tag{18}$$

$$\overline{H}_i(-w) = \int_{-\infty}^{\infty} \overline{h}_j(t_2-\mu_2)e^{-jw(t_2-\mu_2)}\delta\mu_2 \tag{19}$$

The matrix $[\mathbf{S_{F_K}F_L}(\mathbf{w})]$ in (20) donate the turbulent wind loads cross power spectrum matrix; its element $S_{F_K}F_L(w)$ is calculated based on the Davenport wind speed spectrum developed by [29]

$$K, L = 1,2,3,\ldots\ldots n \tag{20}$$

In which P_{KL} represents the coherence function in between the *K*th mass and *i*th mass, and $\mathrm{S_f(w)}$ is the turbulent wind load power spectrum expressed as:

$$S_f(w) = \frac{2x^2}{aw(1+x^2)^{4/3}},\ x = \frac{30}{\sqrt{w_o T}} \tag{21}$$

where w_{o} represents the average wind pressure (10 m above the ground), and T1 represents the period of turbulent wind.

The parameters for the Davenport wind speed spectrum, including the average wind pressure ($\mathrm{w_0}$), are selected in accordance with the Chinese Code for the Design of Building Structures (GB 50009-2012) [30] The average wind pressure $\mathrm{w_0}$ is taken as 0.45 $\mathrm{kN/m^2}$, corresponding to a 50-year return period in a Category B terrain.

Also, from Equation (20) F_{k} is given by

$$F^*{}_k = 1/2\mu\cdot f\mu_s\cdot\mu_\gamma\cdot w_o\cdot A_K,\ K = 1,2,3,\ldots\ldots n \tag{22}$$

In which A_{k} is the tributary area of *K*th mass in the wind course, μ_{s} is the building body type coefficient, μ_f is the fluctuating coefficient, μ_{y} represents the coefficient of wind profiles in the vertical direction, and μ is the peak factor of the turbulent wind.

By using the Fourier transformation, the power spectrum response $S_{z_iz_j}(w)$ can be obtained from Equation (17) as:

$$\begin{gathered} S_{z_iz_j}(w) = H_i(w){m_i}^{i-1}V_i^T[S_{F_K}F_L(w)]\overline{V}_j{m_i}^{1-T}\overline{H}^T(-w) \\ i,j = 1,2,3,\ldots\ldots 2N,\ K,L = 1,2,3,\ldots\ldots n \end{gathered} \tag{23}$$

By further considering the model transformation in Equation (23), the displacement power spectrum of the response matrix S_{x} (w) can be expressed as:

$$S_x(w) = u[S_{z_i z_j}(w)]\overline{u}^T \tag{24}$$

Ultimately, the response value of the displacement mean square can be obtained from

$$\delta x^2 = \int_{-\infty}^{\infty} S_x(w)\delta w \tag{25}$$

2.4. Expression of the Acceleration Power Spectrum Response (APSR) of the Structure

In this case, to derive the APSR and MSR, the cross-variance function of Zi (t) and Zj (t) are represented in Equation (26).

$$\begin{array}{l} E[\frac{dZ_i}{dt}(t_1)\overline{Z}_j{}^T(t_2)] = E\left[F_{Z_i}(t_1)F_{Z_j}{}^{\overline{T}}(t_2)\right] + P_i E\left[Z_i(t_1)\overline{Z_j}^T(t_2)\right]\overline{P_j}^T + \\ E\left[F_{z_i}(t_1)\overline{Z_j}^T(t_2)\right]\overline{P_j}^T + P_i E\left[Z_i(t_1)\overline{F}_{z_j}{}^T(t_2)\right] \end{array} \tag{26}$$

where $F_{z_i}(t) = {m_i}^{i-1}{V_i}^T F(t)$, $i, j = 1, 2, \ldots\ldots 2N$, $E[Z_i(t)\overline{Z}_j{}^T]$ has been defined in Equation (17),

$$E[F_{z_i}(t_1)\overline{F}_{z_j}{}^T(t_2)] = \int_{-\infty}^{\infty} {m_i}^{i-1}{V_i}^T[S_{F_K}F_L(w)]\overline{V}_j{\overline{m}_i}^{i-T}e^{jw(t_2-t_1)}\delta w \tag{27}$$

$$E[F_{z_i}(t_1)\overline{Z}_j{}^T(t_2)] = \int_{-\infty}^{\infty} {m_i}^{i-1}{V_i}^T[S_{F_K}F_{hL}(w)]\overline{V}_j{\overline{m}_i}^{i-T}\overline{H_j}^T e^{jw(t_2-t_1)}\delta w \tag{28}$$

$$\begin{array}{c} E[Z_i(t_1)\overline{F_{z_j}}^T(t_2)] = \int_{-\infty}^{\infty} H_i(-w){m_i}^{i-1}{V_i}^T[S_{F_K}F_L(w)]\times\overline{V}_j{\overline{m}_i}^{i-T}e^{jw(t_2-t_1)}\delta w \\ i, j = 1, 2, 3, \ldots\ldots 2N,\ K, L = 1, 2, 3, \ldots\ldots 2N \end{array} \tag{29}$$

By further considering the Fourier transformation and substituting Equations (17), (23), (27) and (28) into Equation (26), the power spectrum response $S_{\dot{z}_i\dot{z}_j}$

$$\begin{array}{l} S_{\dot{z}_i\dot{z}_j}(w) = {m_i}^{i-1}{V_i}^T[S_{F_K}F_L(w)\overline{V}_j{\overline{m}_i}^{i-T} + P_i H_i(-w){m_i}^{i-1}{V_i}^T[S_{F_K}F_L(w)]\overline{V}_j{\overline{m}_i}^{i-T}\overline{H_j}^T(-w)\overline{P_j}^T \pm \\ {m_i}^{i-1}{V_i}^T[S_{F_K}F_L(w)]\times\overline{V}_j{\overline{m}_i}^{i-T}\overline{H_j}^T(-w)\overline{P_j}^T \pm P_i H_i(-w){m_i}^{i-1}{V_i}^T[S_{F_K}F_L(w)]\overline{V}_j{\overline{m}_i}^{i-T} \\ i, j = 1, 2, 3, \ldots\ldots 2N,\ K, L = 1, 2, \ldots\ldots n \end{array} \tag{30}$$

Therefore, the response spectrum matrix of the acceleration S_{x} (w) can be expressed as:

$$S_{\ddot{x}}(w) = uP\left[S_{\dot{z}_i\dot{z}_j}(w)\right]\overline{P}^T\overline{u}^T \tag{31}$$

Also, the mean square value of the acceleration $\delta_{\ddot{x}^2}$ can be expressed as:

$$\delta_{\ddot{x}^2} = \int_{-\infty}^{\infty} \delta_{\ddot{x}}(w)\delta w \tag{32}$$

3. Numerical Analysis of the Improved MSCSS Under Random Wind Loads

To characterize the dynamic behavior of the MSCSS under non-proportional damping, the natural frequencies and damping ratios of the first three complex modes are obtained using the state-space formulation and are presented in Table 2.

Table 2. Frequencies and damping ratios of the first three modes (RD = 0.3, MR = 1.2).

Mode	Natural Frequency (Hz)	Damping Ratio (ζ_i)
1	0.294	0.023
2	0.688	0.029
3	1.138	0.034

To examine the performance of this improved MSCSS, the control performance of the recommended MSCSS and traditional mega-substructure MSS is compared. The improved arrangement presented in this study is a steel MSCSS based on the traditional mega-sub system (MSS) used in Hong Kong (Bank of China) and City Hall in Tokyo, as illustrated in Figure 1. It is made up of four mega-frames and four eight-floor sub-frames, with the connections seen between the sub-frames and the 2nd, 3rd, and 4th floors of the mega-frames being released. Viscous dampers have also been installed between the mega-structure and the topmost floors of these three (2nd, 3rd, and 4th) sub-frames. Additional columns, as shown in the figure, have also been presented at these same top floors to address the limitations related with the mega beam and mega-floor beam's excessively long span [31]. In addition, rubber bearings were introduced and installed at the top of the additional column to alleviate parallel constraints between the column and the mega floor beam and better the comfort and security of structural and non-structural members under high wind loads by reducing sub-structural response. The two buildings shown in Figure 1 are made up of mega lattice columns and latticed mega beams and are both 144 m high, and each mega floor is 36 m high.

Equation (33) is used to compare the MSCSS and MSS response performance and control effectiveness.

$$\gamma = \frac{R_* - R}{R_*} \tag{33}$$

where γ is the control ratio, and R* and R represent the peak displacement behavior of the building with and without rubber bearings, respectively.

Figure 3's time-history result shows the dynamic reaction of the top mega-structure and sub-frames to wind loading. A numerical analysis of these results, reported in Table 3, shows that the MSCSS has higher control effectiveness when compared to the conventional MSS. The MSCSS reduced peak acceleration at the top mega-structure by 61.02%, from 0.5932 m/s^2 to 0.2312 m/s. Similarly, the displacement in the third and fourth sub-frames was reduced by 52.31% and 45.60%, respectively. Also, as shown in Table 3, the RMS acceleration was reduced by 58.4%, which is statistically significant and ensures a higher level of occupant comfort and serviceability. These significant reduction percentages verify the MSCSS's effectiveness in increasing structural stability, occupant comfort, and the building's overall wind resistance.

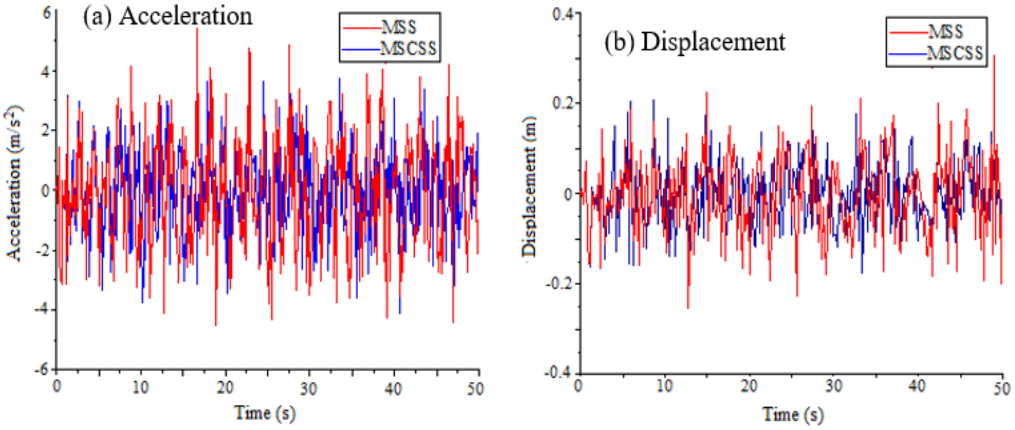


Figure 3. Time history responses at the top of the mega-structure.

Power Spectral Density (PSD) analysis was performed to evaluate the energy distribution in the frequency domain, as shown in Figure 4. The result clearly shows that the MSCSS significantly attenuates the peak energy at the fundamental frequency (0.294 Hz), confirming the 'tuned' absorber effect of the substructures. The energy reduction in the

first mode is approximately 72%, proving the effectiveness of the control mechanism in the frequency range most critical for wind-induced vibration.

Table 3. Maximum value of the response of the MSS and MSCSS models.

Structural Response	MSS	MSCSS	Control Ratio (%)	MSS (RMS)	MSCSS (RMS)	Control Ratio (%)
Top Mega Accel. (m/s^2)	0.5932	0.2312	61.02	0.5932	0.2312	61.02
Top Mega Disp. (m)	0.0371	0.0235	40.34	0.0371	0.0235	40.34
4th Substructure Accel. (m/s^2)	0.8212	0.4125	49.77	0.8212	0.4125	49.77
4th Substructure Disp. (m)	0.0364	0.0198	45.60	0.0364	0.0198	45.60
3rd Substructure Accel. (m/s^2)	0.3275	0.1625	50.38	0.3275	0.1625	50.38
3rd Substructure Disp. (m)	0.0172	0.0082	52.31	0.0172	0.0082	52.31

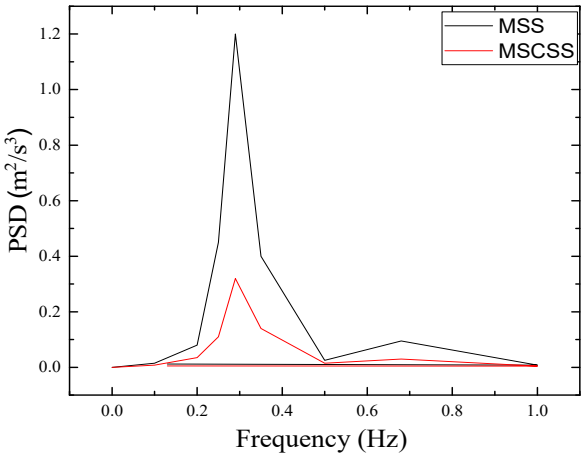


Figure 4. Power Spectral Density (PSD)—Frequency analysis of MSS and MSCSS.

The numerical modeling approach and the complex mode analysis framework employed in this study are validated against established structural dynamics theories [32,33]. While the improved MSCSS configuration is a newly proposed one, the observed behavioral trends align with previous numerical investigations of mega-substructures under seismic and wind actions [31], ensuring that the control performance reported herein is reliable and mathematically sound.

3.1. Dynamic Parameters for MSCSS Responses

To further study the effectiveness of the improved MSCSS with various sub-structural mass and stiffness under heavy wind load, the relative mass ratio and stiffness ratio are defined as follows.

The relative mass ratio (RM):

$$RM = \frac{\sum M_{sub}}{\sum M_{mega}} \tag{34}$$

wherein, M_{sub} represents the sub-structural mass, and M_{mega} is the mega-structural mass.

The sub-structural stiffness ratio (RD) is expressed in Equation (35).

$$RD = \frac{K_{sub}}{K_{mega} \times N_s} \tag{35}$$

where K_{sub} is the inter-floor stiffness of the substructure, which is given in Equation (36), and K_{mega} is the stiffness of the mega-element and is computed from Equation (37):

$$K_{sub} = 0.142 \times 10^6 \times E \times I_{sub} \tag{36}$$

$$K_{mega} = \frac{3EI}{H_{mega}^3} \tag{37}$$

where H_{mega} represents the building height, and N_s is the number of floors in one substructure.

3.2. Effect of the Relative Stiffness Ratio (RD)

The influence of the relative stiffness ratio (RD) on structural response is depicted in Figure 5. For values of RD < 0.17, a sharp decrease in displacement is observed as stiffness increases. In this low-stiffness regime, the substructures lack the necessary restorative force to resist wind-induced deformation; as RD approaches the threshold of 0.17, the sub-frames become more stable, effectively acting as mass dampers for the mega-frame. Beyond RD = 0.17, displacement control remains stable until RD reaches 0.6. In contrast, the acceleration response exhibits less consistency across the RD spectrum. Excellent acceleration control is observed within a narrow range of RD = 0.3 to 0.5. This inconsistency arises because acceleration is highly sensitive to the phase shift between the mega-frame and substructures if the substructures are too flexible (RD < 0.3); it fails to provide sufficient inertial force. On the other hand, when RD > 0.6, the system becomes overly rigid, causing the sub-frames to vibrate, thereby losing the 'out-of-phase' absorber effect and causing the control effectiveness to reduce significantly.

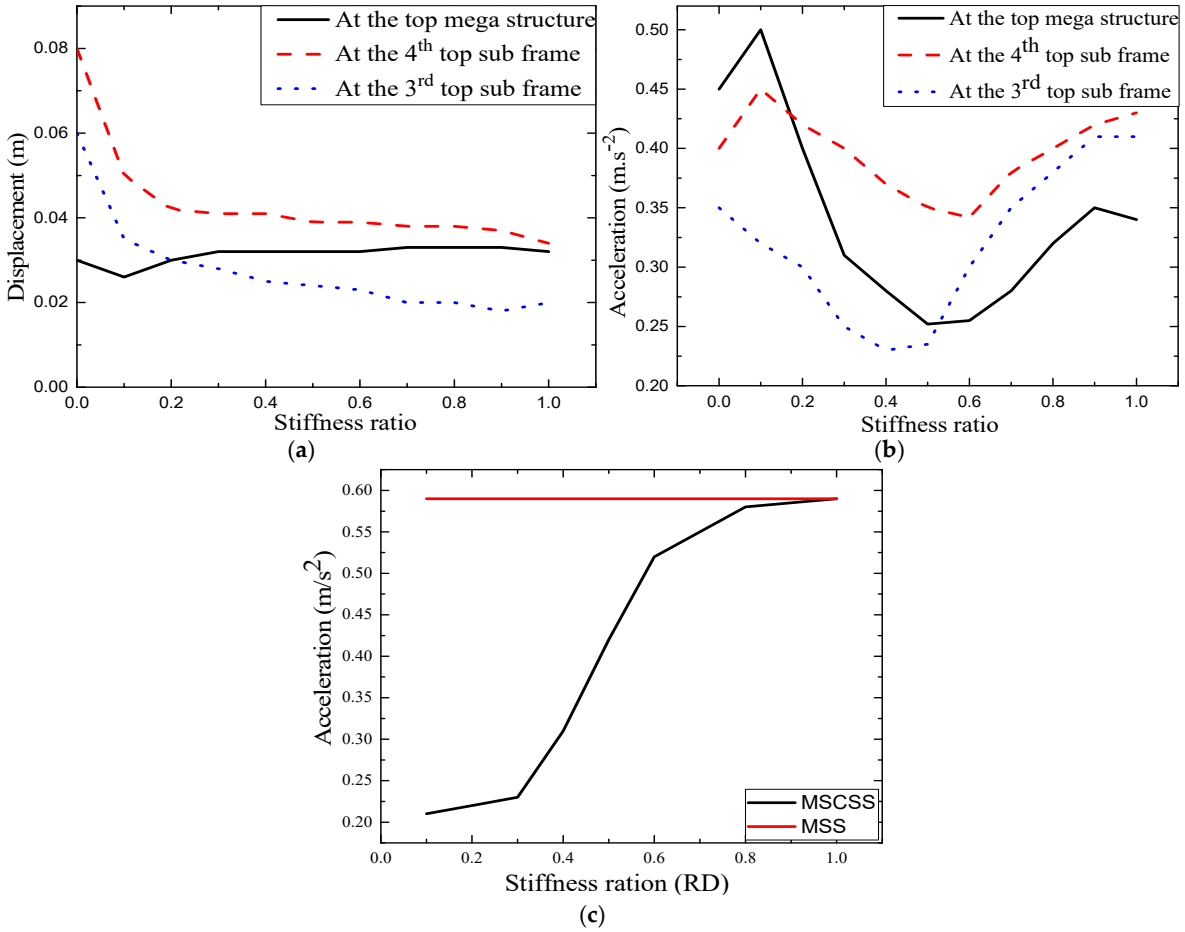


Figure 5. Effect of stiffness ratio on the peak displacement and acceleration response of MSCSS for RM = 1.25. (**a**) Displacement response. (**b**) Acceleleration response. (**c**) Comparative graph showing higher RD values.

3.3. Effect of the Relative Mass Ratio (MR)

The peak displacement and acceleration of the MSCSS exhibited in the third, fourth, and top mega-frames against RM for the stiffness ratio RD = 0.3 are illustrated in Figure 6.

These plots reveal that for RD =0.3, the displacement and acceleration decrease as RM increases, which means that the control effectiveness improves. This trend proves our initial hypothesis that the substructure's mass can be improved to better the control effectiveness of the MSCSS, though the substructure mass increase should not be too much to avoid the deadweight of the system. As depicted in Figure 6, the increasing MR leads to a consistent reduction in the peak responses of the MSCS.

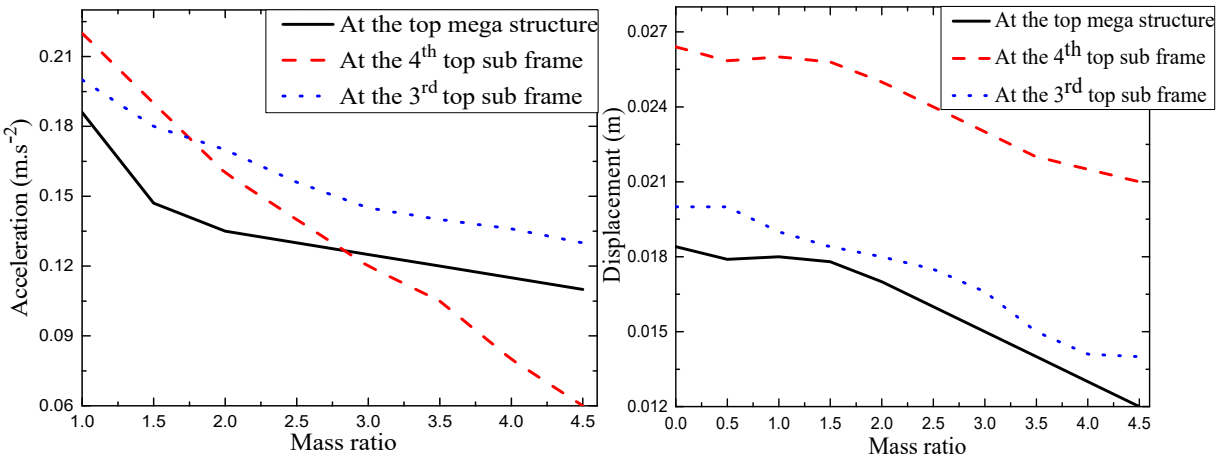


Figure 6. Effect of mass ratio on the peak displacement and acceleration of MSCSS for RD = 0.3.

While increasing the mass ratio MR consistently improves control effectiveness, the optimal upper limit is identified as MR = 1.5. Beyond this value, the control effectiveness diminishes. A detailed weight analysis indicates that at MR = 1.5, the total structural dead load increases by approximately 8.4% compared to the MSS. This increase is considered acceptable within the design safety factors of the mega-columns. However, reaching MR = 2.0 would result in a 15.2% increase in dead load, which may require a costly resizing of the foundation and primary mega-frame members. Therefore, an MR range of 1.0 to 1.5 is recommended for a balanced design.

Also, increasing the mass ratio (MR) results in a slight decrease in the fundamental frequency due to the added inertial mass of the substructures, as shown in Figure 7. The result shows that while the frequency decreases, it remains outside the peak energy range of the Davenport spectrum, preserving control effectiveness.

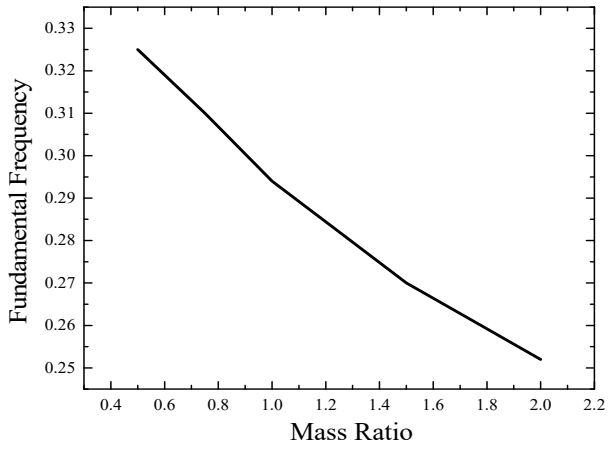


Figure 7. Frequency—mass ratio relationship of MSCSS.

4. Conclusions

In this study, a new design for practical steel MSCSS was presented, highlighting some new ideas to further enhance the performance of the structure building subjected to

random wind load. The control effectiveness and the optimal values of some important parameters that describe the structure's dynamic characteristics are investigated. Based on the analysis result, the following conclusions are drawn:

- The relative stiffness ratio (RD) is an important factor for the control effectiveness of MSCSS. While displacement control remains stable with RD ranges between 0.17 and 0.6, the most improved acceleration control happens when RD is between 0.3 and 0.5. Engineers should avoid RD > 0.6 to achieve improved acceleration control effectiveness of MSCSS.
- The numerical result validates the theory that a higher relative mass ratio, MR, significantly improves the control effectiveness of the structure. This recommends that the MSCSS substructure mass serves as a vibration absorber, provided it does not affect the overall structural effectiveness due to excessive gravity load.
- For practical engineering applications, a stable configuration with RD = 0.4, approximately, is recommended to attain improved control in both displacement and acceleration.
- The study showed that the proposed MSCSS could offer an effective control mechanism when the parameters are appropriately selected as per the guidelines provided based on the analytical study.

Author Contributions: M.A.: Conceptualization, writing—review and editing, methodology, software, formal analysis, Z.X.: investigation, supervision, writing—review and editing, resources, data curation, funding acquisition, B.F.: writing—review and editing, methodology, software, S.I.H.: writing—original draft preparation, visualization, Y.E.I.: project administration, Writing—review and editing, data curation. All authors have read and agreed to the published version of the manuscript.

Funding: This research was funded by National Natural Science Foundation of China (Grant No. 51878274) And The APC was funded by Structures and Materials Laboratory (S&M Lab) at Prince Sultan University's College of Engineering in Riyadh, Saudi Arabia.

Data Availability Statement: Data are contained within the article.

Acknowledgments: The authors would like to acknowledge the financial contributions received from the National Natural Science Foundation of China (Grant No. 51878274), and Structures and Materials Laboratory (S&M Lab) at Prince Sultan University's College of Engineering in Riyadh, Saudi Arabia for paying article publication fee of this research.

Conflicts of Interest: The authors declare no conflicts of interest.

References

1. Housner, G.W.; Bergman, L.A.; Caughey, T.K.; Chassiakos, A.G.; Claus, R.O.; Masri, S.F.; Skelton, R.E.; Soong, T.T.; Spencer, B.F.; Yao, J.T.P. Structural control: Past, present, and future. *J. Eng. Mech.* **1997**, *123*, 897–971. [CrossRef]
2. Al-Subaihawi, S.; Kolay, C.; Marullo, T.; Ricles, J.M.; Quiel, S.E. Assessment of wind-induced vibration mitigation in a tall building with damped outriggers using real-time hybrid simulations. *Eng. Struct.* **2020**, *205*, 110044. [CrossRef]
3. Nava-González, R.; Pozos-Estrada, A.; Lopez-Ibarra, A. Development of Fragility Curves for Tall Buildings with Tuned Liquid Dampers for Vibration Control Under Wind Loading. *Int. J. Civ. Eng.* **2025**, *23*, 57–70. [CrossRef]
4. Alkhatib, F.; Kasim, N.; Goh, W.I.; Shafiq, N.; Amran, M.; Kotov, E.V.; Albaom, M.A. Computational aerodynamic optimization of wind-sensitive irregular tall buildings. *Buildings* **2022**, *12*, 939. [CrossRef]
5. Mazarakou, P.; Papalou, A. Effect of Structural Forms on Wind-Induced Response of Tall Buildings: A Finite Element Approach. *Eng* **2025**, *6*, 131. [CrossRef]
6. Guo, W.; Zhai, Z.; Wang, H.; Liu, Q.; Xu, K.; Yu, Z. Shaking table test and numerical analysis of an asymmetrical twin-tower super high-rise building connected with long-span steel truss. *Struct. Des. Tall Spec. Build.* **2019**, *28*, e1630. [CrossRef]
7. Jafari, M.; Alipour, A. Aerodynamic shape optimization of rectangular and elliptical double-skin façades to mitigate wind-induced effects on tall buildings. *J. Wind. Eng. Ind. Aerodyn.* **2021**, *213*, 104586. [CrossRef]
8. Liu, C.; Xu, D. Diagrid Core-tube Structure Seismic Performance Based on Equivalent Stiffness Ratio of Inner and Outer Tubes. *KSCE J. Civ. Eng.* **2023**, *27*, 1682–1696. [CrossRef]

9. Habrah, A.; Batikha, M.; Vasdravellis, G. An analytical optimization study on the core-outrigger system for efficient design of tall buildings under static lateral loads. *J. Build. Eng.* **2022**, *46*, 103762. [CrossRef]
10. Yao-Qiang, W.; Han, Z.; Haruna, S.I.; Yosri, A.M. Seismic Analyses of Crumb Rubber Concrete Frame Structure Under Four Scenarios. *Arab. J. Sci. Eng.* **2024**, *49*, 5069–5077. [CrossRef]
11. Memon, S.A.; Zain, M.; Zhang, D.; Rehman, S.K.U.; Usman, M.; Lee, D. Emerging trends in the growth of structural systems for tall buildings. *J. Struct. Integr. Maint.* **2020**, *5*, 155–170. [CrossRef]
12. Haque, M.F.; Hossen, I. Numerically evaluate responses of concrete-encased steel tube columns in octal-shaped tall buildings under wind loading. *Results Eng.* **2026**, *29*, 109170. [CrossRef]
13. Jeong, U.Y.; Dupelle, L.; Hartlin, S. Wind load time history regenerated considering coherences for performance-based wind design of tall buildings. *J. Wind. Eng. Ind. Aerodyn.* **2026**, *269*, 106283. [CrossRef]
14. Forcellini, D.; Kalfas, K.N. Inter-story seismic isolation for high-rise buildings. *Eng. Struct.* **2023**, *275*, 115175. [CrossRef]
15. Abdulhadi, M.; Zhang, X.; Atroshchenko, E.; Rungamornrat, J. Enhanced Seismic Resilience of MSCSS Using a Novel Hybrid VD-TFPB Control System with Consideration of SoilStructure Interaction. *Structures 78*, 109094. [CrossRef]
16. Feng, M.Q.; Mita, A. Vibration control of tall buildings using mega subconfiguration. *J. Eng. Mech.* **1995**, *121*, 1082–1088. [CrossRef]
17. Chai, W.; Feng, M.Q. Vibration control of super tall buildings subjected to wind loads. *Int. J. Non-Linear Mech.* **1997**, *32*, 657–668. [CrossRef]
18. Zhang, X.A.; Zhang, J.L.; Jiang, J.S. The Influence of Mega-substructural Stiffness on the Dynamic Property of the Shock-absorption-structure System of Mega-frame. *J. Northwest Polytech. Univ.* **2004**, *22*, 59–63.
19. Li, T.; Zhang, X.; Wang, Q. Control characteristics of mega-sub controlled structure system with friction damper under rare earthquake. In *World Congress on Engineering*; International Association of Engineers: London, UK, 2012; Volume 2189, pp. 791–796.
20. Zhang, X.; Qin, X.; Cherry, S.; Lian, Y.; Zhang, J.; Jiang, J. A new proposed passive mega-sub controlled structure and response control. *J. Earthq. Eng.* **2009**, *13*, 252–274. [CrossRef]
21. Fan, B.; Zhang, X.; Abdulhadi, M.; Wang, Z. Generic optimization, energy analysis, and seismic response study for MSCSS with rubber bearings. *Earthq. Struct.* **2020**, *19*, 347–359.
22. Abdulhadi, M.; Xun'an, Z.; Fan, B.; Moman, M. Evaluation of seismic fragility analysis of the mega sub-controlled structural system (MSCSS). *J. Earthq. Tsunami* **2020**, *14*, 2050025. [CrossRef]
23. Fan, B.; Zhang, X.; Abdulhadi, M.; Moman, M.; Wang, Z. Seismic behavior of MSCSS based on story drift and failure path. *Lat. Am. J. Solids Struct.* **2021**, *18*, e411. [CrossRef]
24. Wang, X.; Zhang, X.; Moman Shahzad, M.; Shi, X. Research on the disaster prevention mechanism of mega-sub controlled structural system by vulnerability analysis. *Structures* **2021**, *33*, 4481–4491. [CrossRef]
25. Abdulhadi, M.; Xun'an, Z.; Fan, B.; Moman, M. Design, optimization and nonlinear response control analysis of the mega sub-controlled structural system (MSCSS) under earthquake action. *J. Earthq. Tsunami* **2020**, *14*, 2050013. [CrossRef]
26. Vaicaitis, R.; Shinozuka, M.; Takeno, M. Parametric study of wind loading on structures. *J. Struct. Div.* **1973**, *99*, 453–468. [CrossRef]
27. Caughey, T.K.; O'Kelly, M.E.J. Classical Normal Modes in Damped Linear Dynamic Systems. *J. Appl. Mech.* **1965**, *32*, 583–588. [CrossRef]
28. Fang, T. *Engineering Random Vibration*; National Defence Industry Press: Beijing, China, 1995.
29. Zhang, X.A.; Jiang, J.S. The random Responses of Internal Forces of Tall TV Towers under wind loads. *J. Northwest Polytech. Univ.* **2020**, *18*, 179–182.
30. *GB 50009-2012*; Load Code for the Design of Building Structures. China Architecture & Building Press: Beijing, China, 2012.
31. Xun'an, Z.; Dong, W.; Jiesheng, J. The controlling mechanism and the controlling effectiveness of passive mega-sub-controlled frame subjected to random wind loads. *J. Sound Vib.* **2005**, *283*, 543–560. [CrossRef]
32. Shahzad, M.M.; Zhang, X.; Wang, X.; Abdulhadi, M.; Wang, T.; Xiao, Y. Response control analysis of a new mega-sub controlled structural system (MSCSS) under seismic excitation. *Struct. Des. Tall Spec. Build.* **2022**, *31*, e1935. [CrossRef]
33. Abdulhadi, M.; Xun'an, Z.; Fan, B.; Moman, M. Substructure design optimization and nonlinear responses control analysis of the mega-sub controlled structural system (MSCSS) under earthquake action. *Earthq. Eng. Eng. Vib.* **2021**, *20*, 687–704. [CrossRef]

Disclaimer/Publisher's Note: The statements, opinions and data contained in all publications are solely those of the individual author(s) and contributor(s) and not of MDPI and/or the editor(s). MDPI and/or the editor(s) disclaim responsibility for any injury to people or property resulting from any ideas, methods, instructions or products referred to in the content.